submitted to *Geophys. J. Int.*

Mantle Q structure from S, SS, SSS and $SSSS$ amplitude measurements

Min Zhu[1,2,3], Shuyang Sun[3], Ying Zhou[3] and Qingju Wu[1]

1: Institute of Geophysics, China Earthquake Administration, Beijing 100081, China

2: Institute of Theoretical and Applied Geophysics, Peking University, Beijing 100087, China

3: Department of Geosciences, Virginia Tech, Blacksburg, VA 24061

Abstract

The seismic quality factor (Q) of the Earth's mantle is of great importance for the understanding of the physical and chemical properties that control mantle anelasticity. The radial structure of the Earth's Q is less well resolved compared to its wavespeed structure, and large discrepancies exist among global 1-D Q models. In this study, we build a global dataset of amplitude measurements of S, SS, SSS and SSSS waves using earthquakes that occurred between 2009 and 2017 with moment magnitudes ranging from 6.5 to 8.0. Synthetic seismograms for those events are computed in a 1-D reference model PREM, and amplitude ratios between observed and synthetic seismograms are calculated in the frequency domain by spectra division, with measurement windows determined based on visual inspection of seismograms. We simulate wave propagation in a global velocity model S40RTS based on SPECFEM3D and show that the average amplitude ratio as a function of epicentral distance is not sensitive to 3-D focusing and defocusing for the source-receiver configuration of the dataset. This dataset includes about 5500 S and SS measurements that are not affected by mantle transition zone triplications (multiple ray paths), and those measurements are applied in linear inversions to obtain a preliminary 1-D Q model QMSI. This model reveals

a high Q region in the uppermost lower mantle. While model QMSI improves the overall datafit of the entire dataset, it does not fully explain SS amplitudes at short epicentral distances or the amplitudes of the SSS and SSSS waves. Using forward modeling, we modify the 1-D model QMSI iteratively to reduce the overall amplitude misfit of the entire dataset. The final Q model QMSF requires a stronger and thicker high Q region at depths between 600 and 900 km. This anelastic structure indicates possible viscosity layering in the mid mantle.

Key words: Structure of the Earth; Body waves; Seismic attenuation

1 INTRODUCTION

It is known that the Earth's crust and mantle is not purely elastic and energy dissipation occurs as seismic waves travel through the Earth's interior. The anelasticity of the solid Earth can be quantified by the seismic quality factor Q, and its inverse $1/Q$ measures energy loss per wave cycle. While mantle anelasticity is very important for the understanding of the thermal and compositional structure of the Earth, the development of global Q models has progresses much slower than seismic wavespeed models, and large discrepancies exit among global Q models (e.g., Bhattacharyya et al. 1996; Billien et al. 2000; Romanowicz & Durek 2000; Selby & Woodhouse 2002; Warren & Shearer 2002; Gung & Romanowicz 2004; Lawrence & Wysession 2006b; Dalton et al. 2008; Savage et al. 2010; Hwang et al. 2011; Ruan & Zhou 2012; Durand et al. 2013; Ma et al. 2016; Karaoglu & Romanowicz 2018).

The depth profile of the earth's anelasticity (Q) structure has been studied since the 1970s based on normal modes as well as surface-wave and body-wave amplitude measurements (e.g., Anderson & Hart 1978; Dziewonski & Anderson 1981; Widmer et al. 1991; Durek & Ekstrom 1996; Lawrence & Wysession 2006a; Oki & Shearer 2008; Hwang et al. 2011; Durand et al. 2013). There is some general agreement in the preliminary structure of the 1-D Q models. In most models, a low Q region exists in the upper mantle at depths corresponding to the weak asthenosphere and Q values are overall higher in the lower mantle

than in the upper mantle. However, the seismic Q structure is far less well resolved compared to the wavespeed structure and large discrepancies exist among published global Q models. For example, Q values in the mantle transition zone are significantly higher in model QM1 (Widmer et al. 1991) than in PREM (Dziewonski & Anderson 1981), and a wide range of Q values have been reported for the lower mantle in different studies (e.g., Anderson & Hart 1978; Dziewonski & Anderson 1981; Widmer et al. 1991; Durek & Ekstrom 1996; Lawrence & Wysession 2006a; Oki & Shearer 2008; Hwang et al. 2011).

In this study, we build a global dataset of amplitude measurements of S, SS, SSS and SSSS waves at epicentral distances between 50° and 125° to investigate the 1-D Q structure of the earth's mantle. This dataset is most sensitive to the Q structure in the mantle transition zone and the shallow lower mantle. The amplitudes of S waves as well as the majority of SS waves are not affected by mantle triplications, they are used in linear inversions to find a preliminary 1-D Q model (QMSI). We use this model as a starting point in forward modeling to obtain a final model that improves the overall datafit to the entire datasets, including multiple-reflected S waves that are affected by mantle triplications. We modify the 1-D Q model iteratively to reduce the overall amplitude misfit, starting with waves turning at shallowest depths. The final Q model (QMSF) confirms the existence of a strong lid (high Q region) in the uppermost lower mantle, indicating possible viscosity layering in the mid mantle as inferred from recent geoid observations (e.g., Rudolph et al. 2015). Finally, we compare model QMSF with several published Q models and discuss limitations in resolving 1-D Q structure using amplitude data.

2 DATA AND AMPLITUDES MEASUREMENTS

We process three-component broadband seismograms recorded at 150 stations from the Global Seismology Network (GSN) for earthquakes occurred between January 2009 and November 2017 with moment magnitudes greater than 6.0. Waveforms with epicentral distance between 50° and 125° are downloaded from the Incorporated Research Institutions for Seismology (IRIS) Data Management Center. The initial processing includes

removing instrument responses, rotation to the great-circle reference frame, and band-pass filtering with corner frequencies at 0.01 and 0.08 Hz. Only transverse-component seismograms are used in this study to investigate shear wave attenuation.

We calculate synthetic seismograms in a 1-D reference model PREM (Dziewonski and Anderson 1981) using travelling-wave mode summation (Liu & Zhou 2016). We use focal mechanism solutions and source time functions from the Global Centroid Moment Tensor Project (Ekstrom et al. 2012). The synthetic seismograms are then filtered to the same frequency range using the same band-pass filter as applied to the observed seismograms. We discard traces with low signal-to-noise ratios as well as traces with no multiple reflected S waves determined by visual inspection. The minimum signal-to-noise ratio of the dataset is 3.2, defined as the ratio of the maximum amplitude of the S wave divided by the absolute value of the maximum background noise measured in a window 80 seconds prior to the start of the S wave measurement window. The observed seismogram with the smallest signal-to-noise ratio is plotted in Figure S1. The final data set includes about 3900 seismograms from 252 earthquake events. This dataset provides a good global coverage in the mantle transition zone and the uppermost lower mantle. Figure 1 shows the distribution of events and seismic stations used in this study as well as ray segments at depths between 400 and 1100 km.

In determining measurement time windows for S, SS, SSS and SSSS waves, we use the theoretical travel times of the seismic phases in model PREM as well as the corresponding synthetic seismograms as references. Cross-correlation time shifts are applied to better align the observed and synthetic seismograms for amplitude measurements when uncertainties in earthquake origin times or locations introduce an overall time shift between the observed and the synthetic seismograms. We adjust the time windows such that interferences from other phases are minimum and the dominant energy of the measurement phase is at the center of the measurement window. Example time windows used for making amplitude measurements are plotted in Figure 2. We measure the relative amplitudes between the observed and the synthetic seismograms in the frequency domain based on

spectral division.

In the frequency domain, the complex spectra of the observed and synthetic seismograms, $o(\omega)$ and $s(\omega)$ can be written as

$$\begin{aligned} o(\omega) &= \int_{-\infty}^{\infty} o(t)e^{-i\omega t}\,dt \;=\; A_{\rm obs}(\omega)e^{-i\phi_{\rm obs}(\omega)}, \\ s(\omega) &= \int_{-\infty}^{\infty} s(t)e^{-i\omega t}\,dt \;=\; A_{\rm syn}(\omega)e^{-i\phi_{\rm syn}(\omega)}, \end{aligned} \tag{1}$$

where $o(t)$ and $s(t)$ are the time domain observed and synthetic seismograms, and $A_{\rm obs}(\omega)$, $\phi_{\rm obs}(\omega)$, $A_{\rm syn}(\omega)$ and $\phi_{\rm syn}(\omega)$ are the amplitude and phase spectra of the observed and synthetic seismograms, respectively. Both $A(\omega)$ and $\phi(\omega)$ are real functions of frequency ω. If we write the observed spectrum as a deviation from the synthetic spectrum, $A_{\rm obs}(\omega) = A_{\rm syn}(\omega) + \delta A(\omega)$, the logarithm of the amplitude spectra ratio provides a rough estimate of the fractional perturbation in amplitude (for small perturbations),

$$\log\left(\frac{A_{\rm obs}}{A_{\rm syn}}\right) = \log\left(\frac{A_{\rm syn}+\delta A}{A_{\rm syn}}\right) = \log\left(1+\frac{\delta A}{A_{\rm syn}}\right) \approx \frac{1}{2.3}\frac{\delta A}{A_{\rm syn}} \tag{2}$$

In this paper, amplitude spectrum ratios between the observed and the synthetic seismograms are calculated for each phase by spectra division at a period of 20 seconds and the measurements $\log\left(A_{\rm obs}/A_{\rm syn}\right)$ of S, SS, SSS and SSSS waves are plotted as a function of epicentral distance in Figure 3. The logarithm is zero when the synthetic and the observed phases have the same amplitude. Measurements that are outside the two standard deviations are plotted in open circles. The measurements of S waves do not include waves diffracted at the core-mantle boundary ($S_{\rm diff}$) and they are only made at epicentral distances smaller than 100°. The multiple-reflected SSSS waves are not well separable from surface waves at distances smaller than 65°. Most of the S wave amplitude perturbations are between -0.4 and 0.44, with a mean value close to zero. For SS waves, most of the amplitude perturbations fall between -0.38 and 0.52, with a mean value larger than zero, indicating that the overall observed amplitudes are larger (or less attenuation) than PREM predictions. This feature is more significant for multiple-reflected SSS and SSSS waves, with the majority of the amplitude measurements above zero.

To investigate the average amplitude measurements as a function of epicentral distance, we plot the mean amplitudes of the measurements in every 10 degree distance range in Figure 4. The mean amplitudes calculated using data within one or two standard deviations show consistent characteristics, except for SSS waves at 60°-70° degree distance range in which the estimated data uncertainty is quite large. The overall Q structure in model PREM can explain the observed average S wave amplitudes at all epicentral distances. However, it does not explain the amplitudes of shallow turning seismic waves, including SS waves at short epicentral distances between 50 and 80 degree, SSS waves at distances between 80 and 120 degree as well as SSSS waves at distances larger than 100 degree. The amplitude observations are self-consistent in that they all suggest waves turning in the mantle transition zone and uppermost lower mantle experience less attenuation than in PREM.

3 LINEAR INVERSION

The S waves in the dataset as well as SS waves at large epicentral distances are not affected by mantle transition zone triplications (multiple ray paths). This subset of the data includes about 5500 S and SS measurements that can be applied in linear inversions to find a preliminary Q structure. In ray theory, the amplitude perturbation of a seismic wave due to a change in the seismic quality factor Q can be written as

$$\log\left(\frac{A_{\text{obs}}}{A_{\text{syn}}}\right) = -\frac{1}{2}\omega \int \frac{1}{c}\left(\frac{1}{Q} - \frac{1}{Q_0}\right) dl, \tag{3}$$

where c is the seismic wave speed, ω is the angular frequency of the wave, and Q_0 and Q are the quality factors in the reference earth model and the perturbed earth model, respectively. The integration is over the ray path.

The above equation can be re-arranged as

$$-\frac{1}{2}\omega \int \frac{1}{c}\frac{1}{Q}\, dl = \log\left(\frac{A_{\text{obs}}}{A_{\text{syn}}}\right) - \frac{1}{2}\omega \int \frac{1}{c}\frac{1}{Q_0}\, dl. \tag{4}$$

In this study, we use S, SS, SSS and SSSS waves that turn either in the mantle transition zone or the lower mantle. Therefore, we will not invert for the Q structure in the upper

mantle but use Q values in the upper mantle from the reference model PREM because the PREM Q structure in the upper mantle is better constrained with a large global dataset including surface waves. In the linear inversion, the reference model is PREM, we use amplitude measurements made with respect to PREM synthetics and solve for perturbations in Q. We parameterize the Q structure in the mantle transition zone and the lower mantle as five layers with a constant Q value in each layer in the following depth range: 400-650 km, 650-800km, 800-950 km, 950-1100 km and 1100-2891 km. The Q values in the layers are independent of each other. The linear problem in Equation (4) can be discretized to find the Q values in each layer

$$\mathbf{A}\mathbf{x} = \mathbf{b}, \tag{5}$$

where $\mathbf{A}$ is the sensitivity matrix constructed from ray path integration, with each row being the sensitivity of the data to $1/Q$ values in each layer, $\mathbf{x}$ is the vector of unknown $1/Q$ values in each layer, and $\mathbf{b}$ is the data vector of amplitude measurements with respect to the attenuation in the reference model. The distance intervals used in the ray path integration range between 5 and 10 km.

We solve the linear inverse problem using least square optimization with norm damping.

$$||\mathbf{A}\mathbf{x} - \mathbf{b}||^2 + \alpha^2||\mathbf{x}||^2 = \text{minimum}, \tag{6}$$

or equivalently as

$$(\mathbf{A}^T\mathbf{A} + \alpha^2\mathbf{I})\,\mathbf{x} = \mathbf{A}^T\mathbf{b}, \tag{7}$$

where α is the norm damping parameter. The number of data is ($\sim$5500) is much larger than the number of unknown parameters (five) to be solved. The inverse problem is well determined and we found the solution not sensitive to the damping applied.

We obtain the solution to the linear inverse problem based on single value decomposition (SVD). The tradeoff curve is plotted in Figure S2 and the Q model (QMSI) from the linear inversion is shown in Figure 5. The ray density of the dataset used in the inversion is plotted in every 100 km depth interval, and it shows that Q structure in the mantle transition zone and the uppermost lower mantle at depths between 400 and 1500 km is well sampled by the dataset. The most striking feature in model QMSI is a high Q region

in the uppermost lower mantle at depths between 650 and 800 km, and a low Q region below at depths between 800-1100 km. In the mantle transition zone between 400 and 650 km, the Q value is larger in QMSI than in the reference model PREM, while in the lower mantle at depths greater than 1100 km, Q value in QMSI is smaller than that in PREM.

To quantify the improvement of model QMSI made on the overall amplitude datafit, we calculate synthetic seismograms in model PREM with its attenuation structure replaced by model QMSI. We make amplitude measurements using the same procedure but now with respect to the synthetics generated for model QMSI (Figure 6). There is no significant difference between PREM and QMSI measurements in their mean S wave amplitude datafits, indicating that the accumulated attenuation along the S-wave ray paths in the two models (PREM and QMSI) are about the same. The higher Q values at depths between 650 km and 800 km in model QMSI improve datafit of the SS waves at epicentral distances between 55 and 85 degree, which roughly correspond to rays turning between 700 km and 1000 km depths. In addition, it significantly improves the datafit of SSS and SSSS waves that were not used in the linear inversion. The majority of the triplicated SSS and SSSS waves turn at depths roughly between 400 and 900 km and they do not satisfy the linear relation in Equation (3). This improved datafit is not surprising because the SSS and SSSS waves sample the same mantle transition zone and the uppermost lower mantle multiple times.

4 FORWARD MODELING

In model QMSI, the majority of the SSS and SSSS wave measurements are affected by triplications associated with the 410-km and 660-km discontinuities and therefore they can not be included in the linear inversion. Triplicated waves provide extensive sampling of the structure in the mantle transition zone and the uppermost lower mantle, and they can be studied using forward modeling (e.g., Tajima & Grand 1995; Lai et al. 2019; Zhang et al. 2019). To better constrain the 1-D Q structure in the mantle using the entire amplitude dataset, we use model QMSI as a starting model and apply forward model-

ing to obtain a 1-D Q model that can provide better datafit to S, SS, SSSS and SSSS measurements. We start with adjusting Q values in the shallow mantle transition zone to improve the data fit of the shallow turning waves, followed by Q value perturbations at greater depths. We use turning depths of the ray paths as a reference but understand seismic waves are sensitive to structures off the ray paths and their Fresnel zones often extend a couple of hundred kilometers above and below the turning depths. We calculate synthetic seismograms for every perturbed 1-D Q model, make amplitude measurements and examine the mean amplitude perturbations as a function of epicentral distance. The forward modeling approach is applied iteratively until the final model fits the amplitude dataset reasonably well. The final model (QMSF) is plotted in Figure 7. It confirms that a Q value higher than that in PREM is required in the mantle transition zone between 450 and 600 km depth. In addition, it reveals a thicker and stronger high-Q lid (Q=800) in the uppermost lower mantle at depths between 600 to 900 km. The final model also suggests a weak layer below the high-Q lid with a Q value of 210 at depths between 900 and 1200 km. In the deep lower mantle, Q value is 280 in model QMSF, smaller than the value in PREM but close to the Q value in model QMSI.

The final model QMSF fits the entire dataset better than model QMSI. In particular, it improves the datafit of SS waves at small epicentral distances as well as SSS and SSSS waves that all turn in the mantle transition zone and the uppermost lower mantle. It does not fit well SSS amplitude measurements at the distance range between 60 and 70 degree. This is not unexpected as the uncertainty estimated from data using one and two standard deviations was large for SSS waves at this epicentral distance range (Figure 4).

5 DISCUSSION

In this study, we have focused on the global average of the Q structure by investigating the mean values of the amplitude perturbations of the S, SS, SSS and SSSS waves. It is important to realize that differences in amplitudes between an observed seismogram and a synthetic seismogram calculated in a 1-D wavespeed model (PREM) may come from uncertainties in seismic source parameters as well as 3-D elastic focusing and defocusing.

Uncertainties in source parameters such as earthquake size estimates are expected to be averaged out when the mean amplitudes are calculated from a statistically significant number of data points. For example, any single earthquake in the GCMT catalogue may have an over-estimated or under-estimated scalar moment, and the observed amplitudes from that earthquake will be smaller (or larger) than the GCMT synthetics. In this study, we use mean amplitude measurements averaged over a large number of earthquakes (some earthquakes are over-estimated while others are under-estimated). This averaging minimizes the impact of the uncertainties in the GCMT scalar moment. In addition, systematic over-estimates (or under-estimate) in earthquake magnitudes can be identified as they will introduce the same bias on S, SS, SSS and SSSS waves, which was not observed in this dataset.

Lateral variations in seismic wave speed affect amplitudes through focusing and defocusing. To investigate possible effects of focusing and defocusing on the mean amplitude ratios, we compute synthetic seismograms in a global 3-D wavespeed model S40RTS (Ritsema et al. 2011) using SPECFEM3D (Komatitsch & Tromp 2002) for the same source-receiver configuration of the dataset. The global crustal model is not incorporated in the simulations. This is because incorporating a 3-D crustal structure with the global CMT solutions can be problematic for source excitations as the CMT solutions are obtained assuming PREM crustal structure (Ekstrom et al. 2012) (Figure S4). It is known that lateral variations in crustal thickness may have a significant impact on the traveltimes of the multiple reflected waves but the impact on their amplitudes is limited because amplitudes are sensitive to the second derivatives of structure perturbations not the perturbations themselves (Zhou et al. 2004) (Figure S4 & S5). We make amplitude measurements between seismograms computed for models S40RTS and PREM using the same time windows as in Figure 3. The measurements are plotted in Figure 9 and they show similar characteristics as seen in the real data — waves reflected in the mantle multiple times experience larger variations in amplitudes. The variations are overall smaller than those observed in real data, as the synthetic experiment only accounts for the focusing and defocusing effects in a 3-D wavespeed model, it does not include variations

associated data noise or uncertainties in source parameters. In addition, the 3-D earth model S40RTS may be a smoothed (damped) version of the wavespeed structure in the Earth. We calculate the mean amplitude perturbations in the same 10-degree distance range as applied in the real data and plot them as a function of epicentral distance for S, SS, SSS and SSSS waves in Figure 10. The calculations show that the mean amplitudes due to mantle focusing and defocusing are in general smaller than the uncertainties associated with the average amplitude perturbations estimated from the real data. The SPECFEM3D simulations confirm that the observed large amplitude perturbations of the SS, SSS and SSSS waves can not be explained by mantle wavespeed anomalies but require less attenuation (high Q) in the mantle transition zone and the uppermost lower mantle.

Higher Q values (less attenuation) than PREM in the mantle have been suggested in several published 1-D global Q models. In Figure 11, we compare model QMSF from this study with QM1 (Widmer et al. 1991) and OS08 (Oki & Shearer 2008). PREM Q values are also plotted as a reference. Model QM1 shares some similarity with model QMSF in that it has high Q values in the mantle transition zone as well as in the uppermost lower mantle. The high-Q region in the lower-mantle in model QM1 is much thicker, extending down to ∼1900 km, while the high-Q region in model QMSF is much stronger but has a limited depth extent (600-900 km). Model OS08 has a two-layer structure, with a much smaller Q value in the upper mantle and a much higher Q value in the lower mantle.

We calculate synthetic seismograms in the two 1-D Q models, QM1 and OS08, and measure amplitude ratios between the observed and synthetic seismograms following the same process as applied in the PREM and QMSF synthetics, the mean amplitude ratios are then calculated for S, SS, SSS and SSSS waves. In Figure 12, we compare the mean amplitude ratios in every 10-degree distance range calculated using the same observed seismograms but different synthetics computed using the four reference Q models: PREM, QMSF, OS08 and QM1. The mean amplitude of the observed S waves are smaller than that in model QM1, indicating that the accumulated attenuation of the

S waves in model QM1 is not sufficient to explain the amplitude data, or the overall Q values in model QM1 are too high for S waves. The same applies to deep-turning S waves in model OS08. Model QM1 explains the SS wave amplitude reasonably well, but it does not explain the amplitudes of SSS and SSSS waves, which require less attenuation (higher Q values) in the mantle transition zone and uppermost lower mantle. The Q value is too low in the mantle transition zone in model OS08, and the observed SS, SSS and SSSS amplitudes are much larger than model predictions. It is important to point out that model QM1 was obtained using long-period normal mode data and model OS08 was derived from inversions of body-wave amplitudes at periods between about 3 and 10 s. In this paper, we have used S, SS, SSS and SSSS amplitude measurements at a period of 20 seconds. It is possible that frequency-dependent Q may explain some of the discrepancies and further investigations would require frequency-dependent amplitude measurements. However, frequency-dependent seismic attenuation may not explain the entire discrepancies because the observed S-wave amplitudes are smaller than model predictions while the observed amplitudes of SSS and SSSS waves are larger than model predictions in QM1 and OS08 (Figure 12). This indicates that significant amplitude discrepancies come from differences in the depth-dependent Q structure.

6 CONCLUSIONS

In this paper, we build a global dataset of S, SS, SSS and SSSS amplitude measurements at a period of 20 seconds. S and SS amplitude measurements that are not affected by mantle triplications are applied in linear inversions to obtain a preliminary 1-D global Q structure in the mantle (QMSI). Using model QMSI as a starting model, we take advantage of the multiple-reflected S waves that sample the mantle transition zone and the uppermost lower mantle multiple times and apply the entire amplitude dataset in forward modeling to construct a final Q model (QMSF). Our final Q model QMSF confirms the most prominent feature in model QMSI — a high-Q lid in the uppermost lower mantle. This high Q region is stronger and thicker in model QMSF than in model QMSI, with a Q value of 800 extending from 600 to 900 km depth. The mantle below the high-Q lid is much weaker with a Q value of 210 at depths between 900 and 1200 km. This

observation supports the existence of possible viscosity layering in the mid mantle at a global scale (e.g., Rudolph et al. 2015), probably associated with a change in grain size Jackson et al. (2002) or water content (e.g., Karato 2011; Zhu et al. 2013).

Most of the multiple-reflected S waves used in this study have turning depths either in the mantle transition zone or in the lower mantle. The resolution in the upper mantle is limited and we have adopted the Q structure in the upper mantle from model PREM in both the inversion and the forward modeling. We use a stripping-layer approach in forward modeling to update the Q model iteratively: (1) we start with waves turning at the shallowest depths such that there is no tradeoff from any deeper structure, and we adjust the Q value in the shallowest layer in the mantle transition zone to fit the data until any further perturbations in Q will only reduce the datafit; (2) we then adjust the Q value in the next layer based on trail and error and repeat the same process for waves turning deeper. The final Q model QMSF explains the S, SS, SSS and SSSS amplitude data at 20-second period better than PREM and several other Q models that are also associated with high Q values in the lower mantle. This is not surprising as the main observation in this study is that waves turning in the mantle transition zone and the uppermost lower mantle have large amplitudes (less attenuation), while those turning shallower or deeper have amplitudes close to normal.

The main difference between model QMSF and PREM is the Q structure in the mantle transition zone and the uppermost lower mantle, which does not produce measurable differences on surface-wave or P-wave amplitudes (Figure S6). The amplitudes of multiple-reflected S waves in general provide best constraints on the Q structure at those depths. It is worth noting that model QMSF represents one possible model that can explain the multiple-reflected S waves observed in this study, and approaches similar to Resovsky et al. (2005) may be explored in the future to investigate possible range of models. The depth resolution of our Q model QMSF is limited and can be improved with a larger dataset, for example, if averaging in every 5° becomes statistically sufficient, then the depth resolution can be doubled. In the future, the study can also be extended to include

core phases (ScS, Sdiff) to improve the Q structure in the lowermost mantle. In addition, the anelasticity (Q) of the mantle introduces physical dispersion, while using traveltime measurements to constrain Q structure can be challenging as seismic traveltimes also depend on the velocity structure but the dual dependence may be accounted in joint inversions of seismic traveltimes and amplitudes (e.g., Zhou 2009; Ruan & Zhou 2010).

ACKNOWLEDGMENTS

We thank the Editor Dr. Ebru Bozdag and two anonymous reviewers for their constructive comments, which helped improve the manuscript. The facilities of the IRIS Data Management System, and specifically the IRIS Data Management Center, were used for access to waveform and metadata required in this study. The authors acknowledge Advanced Research Computing at Virginia Tech for providing computational resources and technical support. This research was supported by the US National Science Foundation under Grants EAR-2017218 and National Natural Science Foundation of China with Grant No.41874112. All figures were generated using the Generic Mapping Tools (GMT) (Wessel & Smith 1995).

Data Availability

Seismic Data used in this research are available from the IRIS Data Management Center (http://www.iris.edu).

REFERENCES

Anderson, D. L. & Hart, R. S., 1978. Q of the earth, *J. Geophys. Res.*, **83**, 5869–5882.

Bhattacharyya, J., Masters, G., & Shearer, P., 1996. Global lateral variations of shear wave attenuation in the upper mantle, *J. Geophys. Res.*, **101**, 22273–22289.

Billien, M., Leveque, J.-J., & Trampert, J., 2000. Global maps of rayleigh wave attenuation for periods between 40 and 150 seconds, *Geophys. Res. Lett.*, **27**, 3619–3622.

Dalton, C. A., Ekström, G., & Dziewonski, A. M., 2008. The global attenuation structure of the upper mantle, *J. Geophys. Res.*, **113**, doi:10.1029/2007JB005429.

Durand, S., Matas, J., Ford, S., Ricard, Y., Romanowicz, B., & Montagner, J.-P., 2013. Insights from scs–s measurements on deep mantle attenuation, *Earth and Planetary Science Letters*, **374**, 101–110.

Durek, J. J. & Ekstrom, G., 1996. A radial model of anelasticity consistent with long-period surface-wave attenuation, *Bull. Seismol. Soc. Am.*, **86**(1A), 144–158.

Dziewonski, A. & Anderson, D., 1981. Preliminary reference Earth model *, *Phys. Earth Planet. Inter.*, **25**, 297–356.

Ekstrom, G., Nettles, M., & Dziewoński, A. M., 2012. The global cmt project 2004–2010: Centroid-moment tensors for 13,017 earthquakes, *Physics of the Earth and Planetary Interiors*, **200-201**, 1–9.

Gung, Y. & Romanowicz, B., 2004. Q tomography of the upper mantle using three-component long-period waveforms, *Geophys. J. Int.*, pp. doi:10.1111/j.1365–246X.2004.02135.x.

Hwang, Y. K., Ritsema, J., & Goes, S., 2011. Global variation of body-wave attenuation in the upper mantle from teleseismic p wave and s wave spectra, *Geophysical Research Letters*, **38**, doi:10.1029/2011GL046812.

Jackson, I., Gerald, J. D. F., Faul, U. H., & Tan, B. H., 2002. Grain-size-sensitive seismic wave attenuation in polycrystalline olivine, *JOURNAL OF GEOPHYSICAL RESEARCH*, **107**, doi:10.1029/2001JB001225.

Karaoglu, H. & Romanowicz, B., 2018. Inferring global upper-mantle shear attenuation structure by waveform tomography using the spectral element method, *Geophysical Journal International*, **213**, 1536–1558.

Karato, S., 2011. Water distribution across the mantle transition zone and its implication for global material circulation, *Earth Planet. Sci. Lett.*, **301**, 413–423.

Komatitsch, D. & Tromp, J., 2002. Spectral-element simulations of global seismic wave propagation-I. Validation, *Geophys. J. Int.*, **149**, 390–412.

Lai, Y., Chen, L., Wang, T., & Zhan, Z., 2019. Mantle transition zone structurebeneath northeast asia from 2-dtriplicated waveform modeling: Implication for a segmented stagnant slab, *Journal of Geophysical Research*, **124**, 1871–1888.

Lawrence, J. F. & Wysession, M. E., 2006a. QLM9: A new radial quality factor (Qu) model for the lower mantle, *Earth Planet. Sci. Lett.*, **241**, 962–971.

Lawrence, J. F. & Wysession, M. E., 2006b. Seismic evidence for subduction-transported water in the lower mantle, *Geophysical Monograph Series 168: Earth's deep water cycle*, p. DOI: 10.1029/168GM19.

Liu, K. & Zhou, Y., 2016. Global Rayleigh wave phase-velocity maps from finite-frequency tomography, *Geophys. J. Int.*, **205**, 51–66.

Ma, Z., Masters, G., & Mancinelli, N., 2016. Two-dimensional global rayleigh wave attenuation model by accounting for finite-frequency focusing and defocusing effect, *Geophys. J. Int.*, **204**, 631–649.

Oki, S. & Shearer, P. M., 2008. Mantle Q structure from S-P differential attenuation measurements, *J. Geophys. Res.*, **113**, B12308.

Resovsky, J., Trampert, J., & Van der Hilst, R. D., 2005. Error bars for the global seismic q profile, *Earth and Planetary Science Letters*, **230**, 413– 423.

Ritsema, J., Deuss, A., van Heijst, H. J., & Woodhouse, J. H., 2011. S40RTS: a degree-40 shear-velocity model for the mantle from new Rayleigh wave dispersion, teleseismic traveltime and normal-mode splitting function measurements, *Geophys. J. Int.*, **184**, 1223–1236.

Romanowicz, B. & Durek, J. J., 2000. Seismological constraints on attenuation in the Earth: A review, *Geophysical Monograph Series*, **117**, 161–179.

Ruan, Y. & Zhou, Y., 2010. The effects of 3-d anelasticity(q) structure on surface-wave phase delays, *Geophys. J. Int*, **181**, 479–492.

Ruan, Y. & Zhou, Y., 2012. The effects of 3-d anelasticity(q) structure on surface-wave amplitudes, *Geophys. J. Int*, **189**, 967–983.

Rudolph, M. L., Leki, V., & Lithgow-Bertelloni, C., 2015. Viscosity jump in Earths mid-mantle, *Science*, **350**, 1349–1352.

Savage, B., Komatitsch, D., & Tromp, J., 2010. Effects of 3d attenuation on seismic wave amplitude and phase measurements, *Bulletin of the Seismological Society of America*, **100**, 1241–1251.

Selby, N. D. & Woodhouse, J. H., 2002. The q structure of the upper mantle: Constraints from rayleigh wave amplitudes, *J. Geophys. Res.*, **107**, doi:10.1029/2001JB000257.

Tajima, F. & Grand, S. P., 1995. Evidence of high velocity anomalies in the transition zone associated with southern kurile subduction zone, *Geophysical Research Letters*, **22**, 3139–3142.

Warren, L. & Shearer, P., 2002. Mapping lateral variations in upper mantle attenuation by stacking p and pp spectra, *J. Geophys. Res.*, **107**, doi:10.1029/2001JB001195.

Wessel, P. & Smith, W. H. F., 1995. New version of the generic mapping tools released, *Eos Trans. AGU*, **76**, 329.

Widmer, R., Masters, G., & Gilbert, F., 1991. Spherically symmetric attenuation within the Earth from normal mode data, *Geophys. J. Int.*, **104**, 541–553.

Zhang, M., Sun, D., Wang, Y., & Wu, Z., 2019. Fine structure of the 660-km discontinuity beneath southeastern china, *Geophysical Research Letters*, **46**, 7304–7314.

Zhou, Y., 2009. Surface-wave sensitivity to 3-d anelasticity (q), *Geophys. J. Int*, **178**, 1403–

1410.

Zhou, Y., Dahlen, F. A., & Nolet, G., 2004. 3-d sensitivity kernels for surface-wave observables, *Geophys. J. Int*, **158**, 142–168.

Zhu, H., Bozdag, E., Duffy, T. S., & Tromp, J., 2013. Seismic attenuation beneath europe and the north atlantic:implications for water in the mantle, *Earth and Planetary Science Letters*, **381**, 1–11.

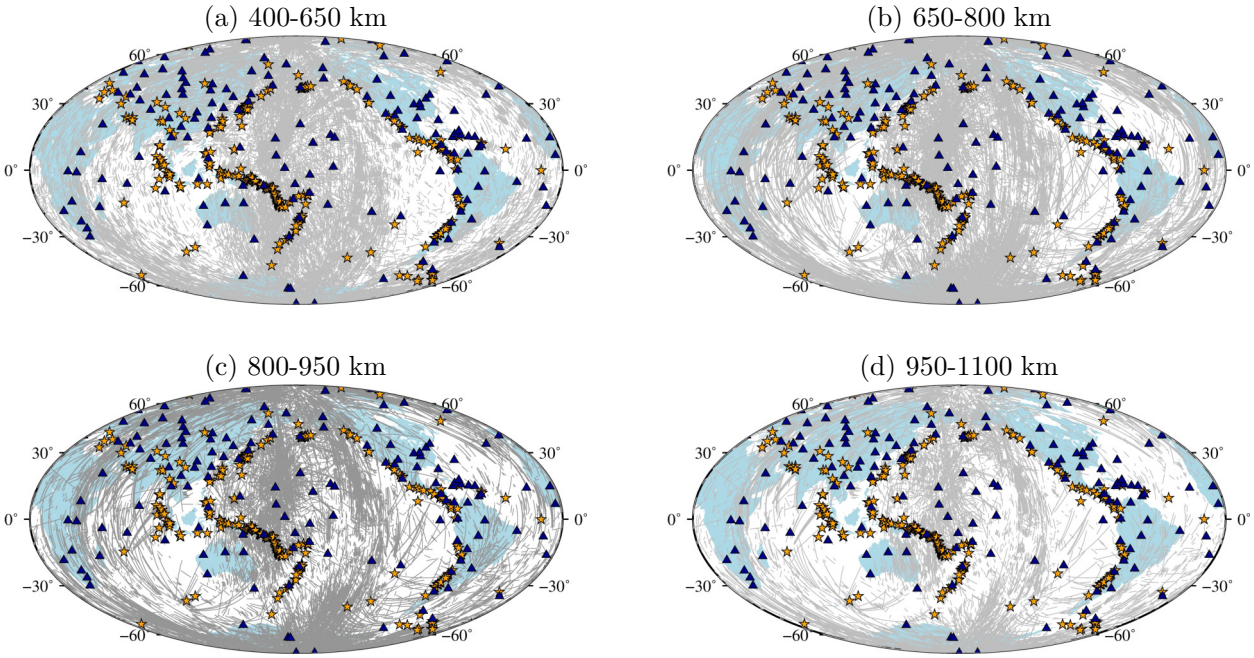

Figure 1. ray-path coverage at different depth ranges for the dataset used in this study: (a) 400-650 km, (b) 650-800 km, (c) 800-950 km and (d) 950-1100 km. The triangles denote the 150 GSN stations and the stars represent the 252 earthquake events used in this study.

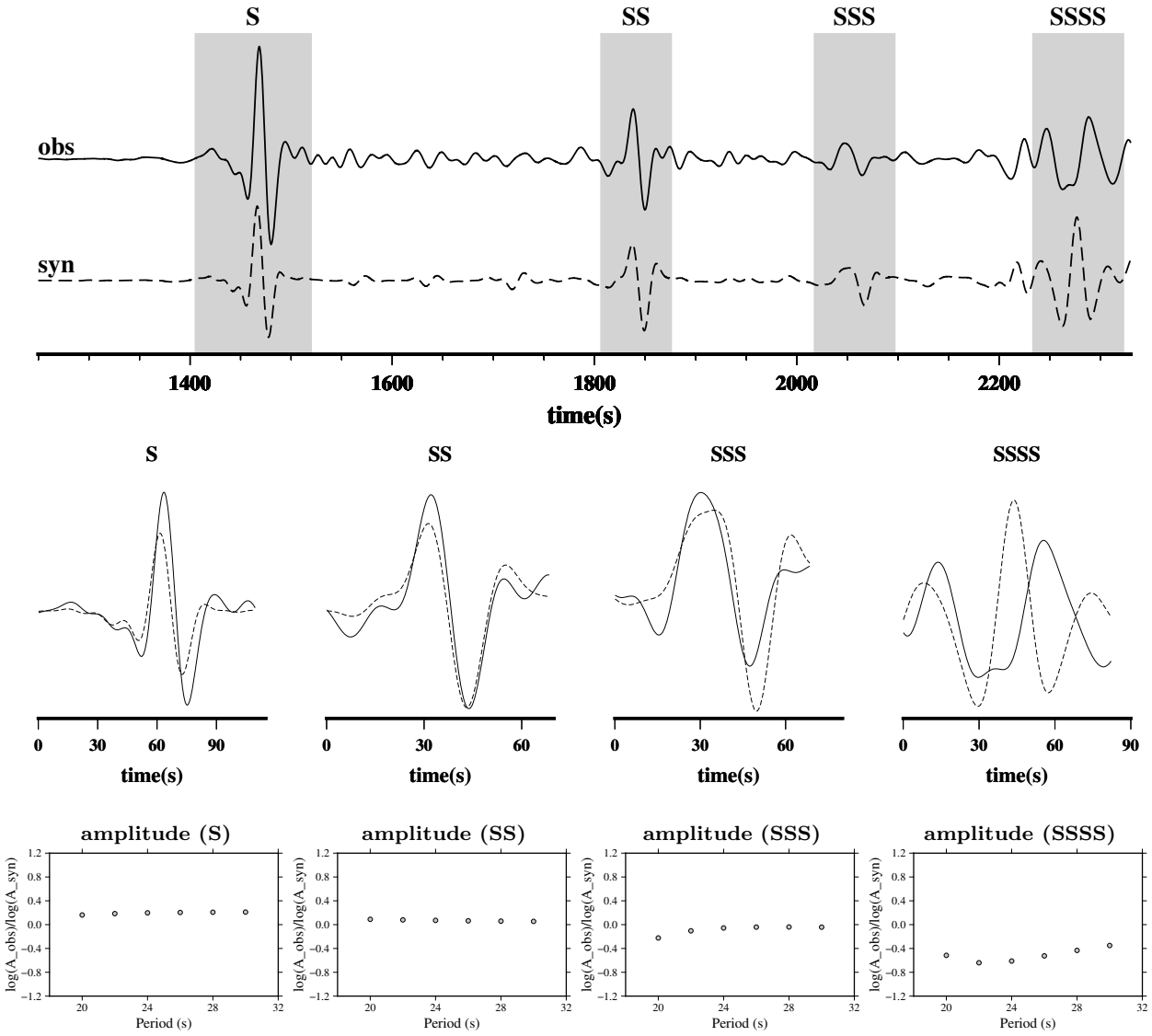

Figure 2. Example time windows and amplitude measurements. Top: example observed and synthetic seismograms recorded at station NNA for a Tonga Islands earthquake occurred on December 4, 2017. The moment magnitude of the earthquake is Mw=6.7. The time windows used for making amplitude measurements of S, SS, SSS and SSSS waves are shaded, and the zoom-in views of the observed (solid line) and synthetic (dashed line) phases are plotted in the middle panels. The bottom panels illustrate the frequency dependence of amplitude measurements of the seismic phases, they are plotted for reference only. We emphasize that frequency-dependent Q is not investigated in the study. The Q models obtained in this study are for seismic waves at a period of 20 seconds, obtained using amplitude measurements at 20-second period only.

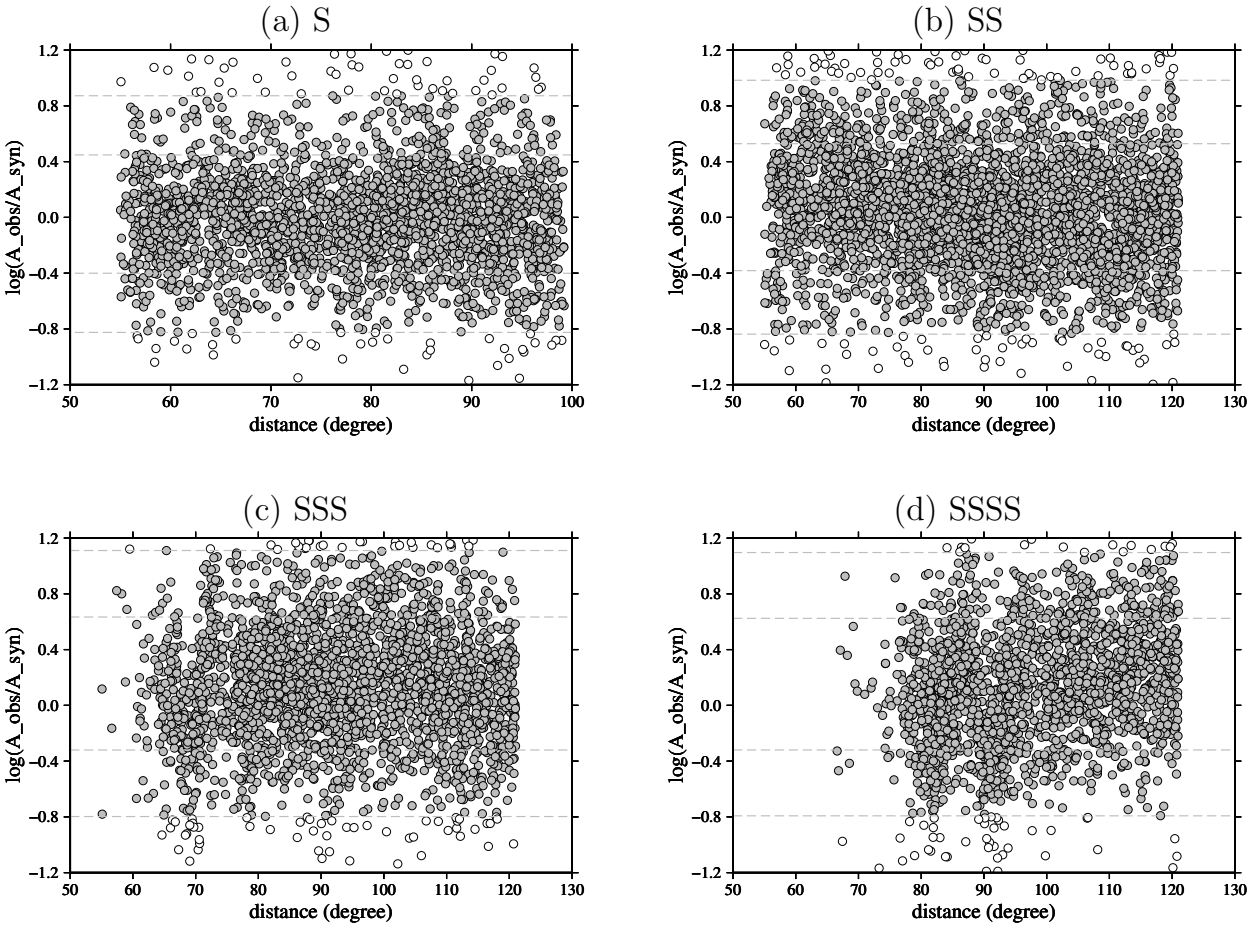

Figure 3. Amplitude measurements $\log(A_{\rm obs}/A_{\rm syn})$ of S, SS, SSS and SSSS waves plotted as a function of epicentral distance at a period of 20 seconds. The logarithm is zero when the synthetic and the observed phases have the same amplitude. The synthetic seismograms are calculated in a reference model PREM. The dashed lines indicate one and two standard deviations of the datasets.

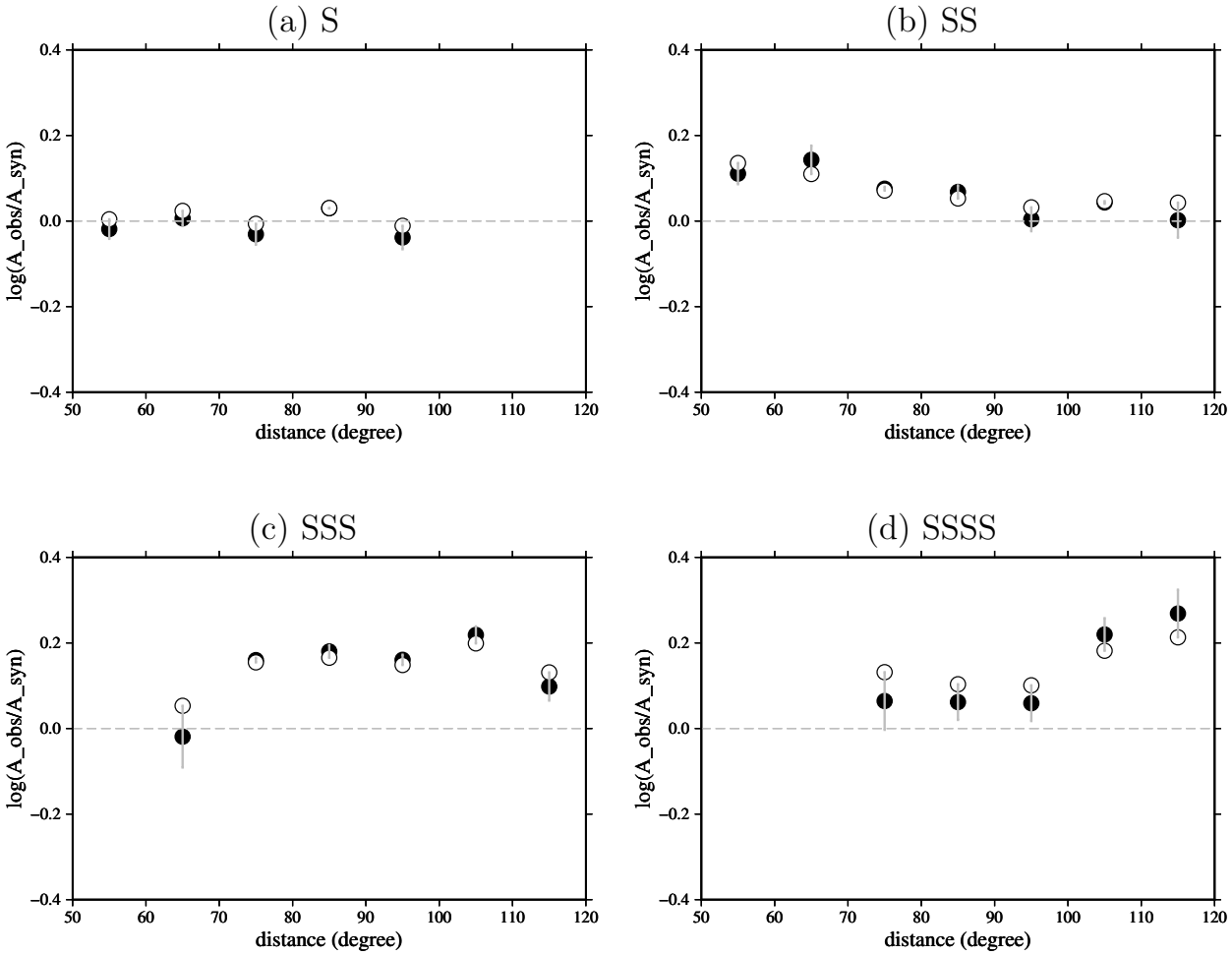

Figure 4. Mean values of the amplitude measurements in every 10° epicentral distance range for (a) S, (b) SS, (c) SSS and (d) SSSS waves. Solid circles are the mean values calculated using measurements within two standard deviations, and open circles are calculated using measurements within one standard deviation. The vertical bars on the solid circles indicate differences between the two estimates.

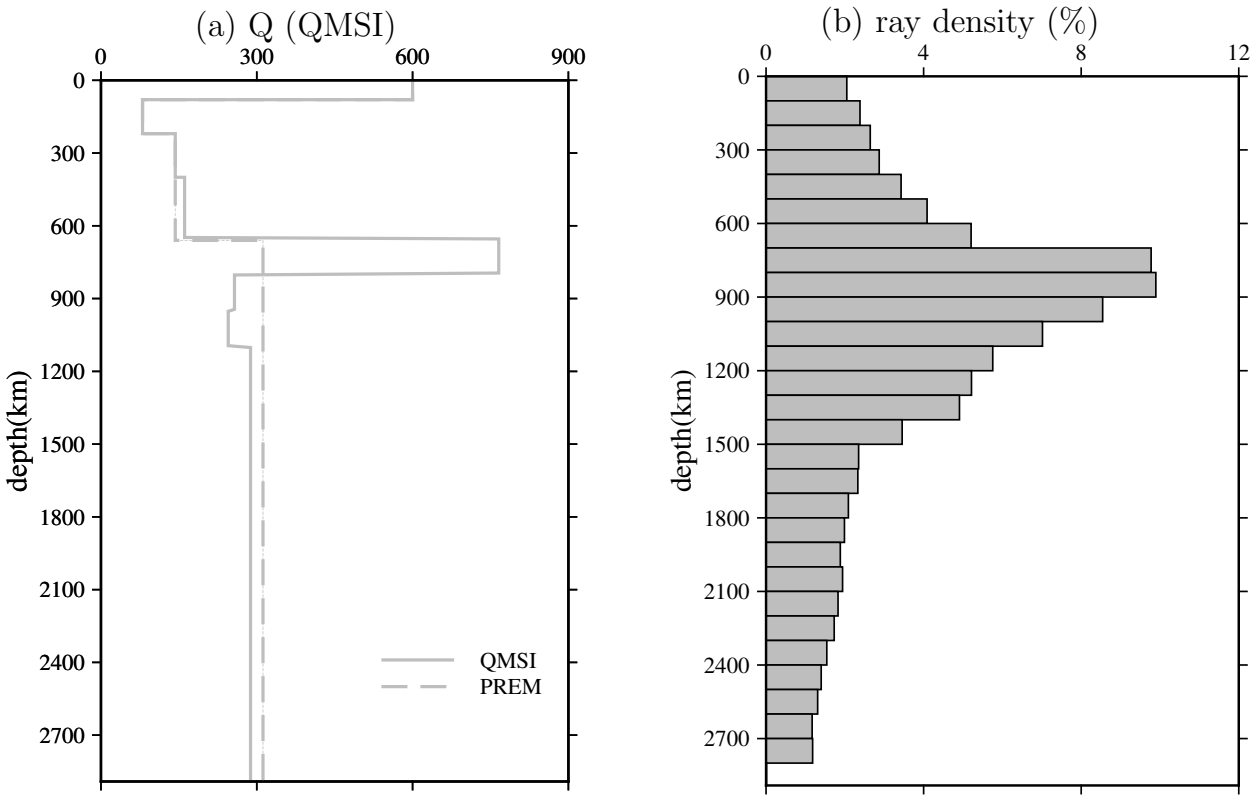

Figure 5. (a) Model QMSI obtained from linear inversion using amplitude measurements of S and SS waves that are not affected by mantle triplications. Model PREM is plotted in dashed line for reference. (b) the percentage of ray paths sampling every 100 km depth range. In QMSI inversion, Q values in the top 400 km of the model are the same as in model PREM, and we invert for Q values in the following layers: 400-650 km, 650-800 km, 800-950 km, 950-1100 km and 1100-2891 km. The linear inversion reveals a high-Q region at depths between 650 and 800 km, and a low Q region between 800 and 1100 km. Q values at depths greater than 1100 km is lower than that in PREM.

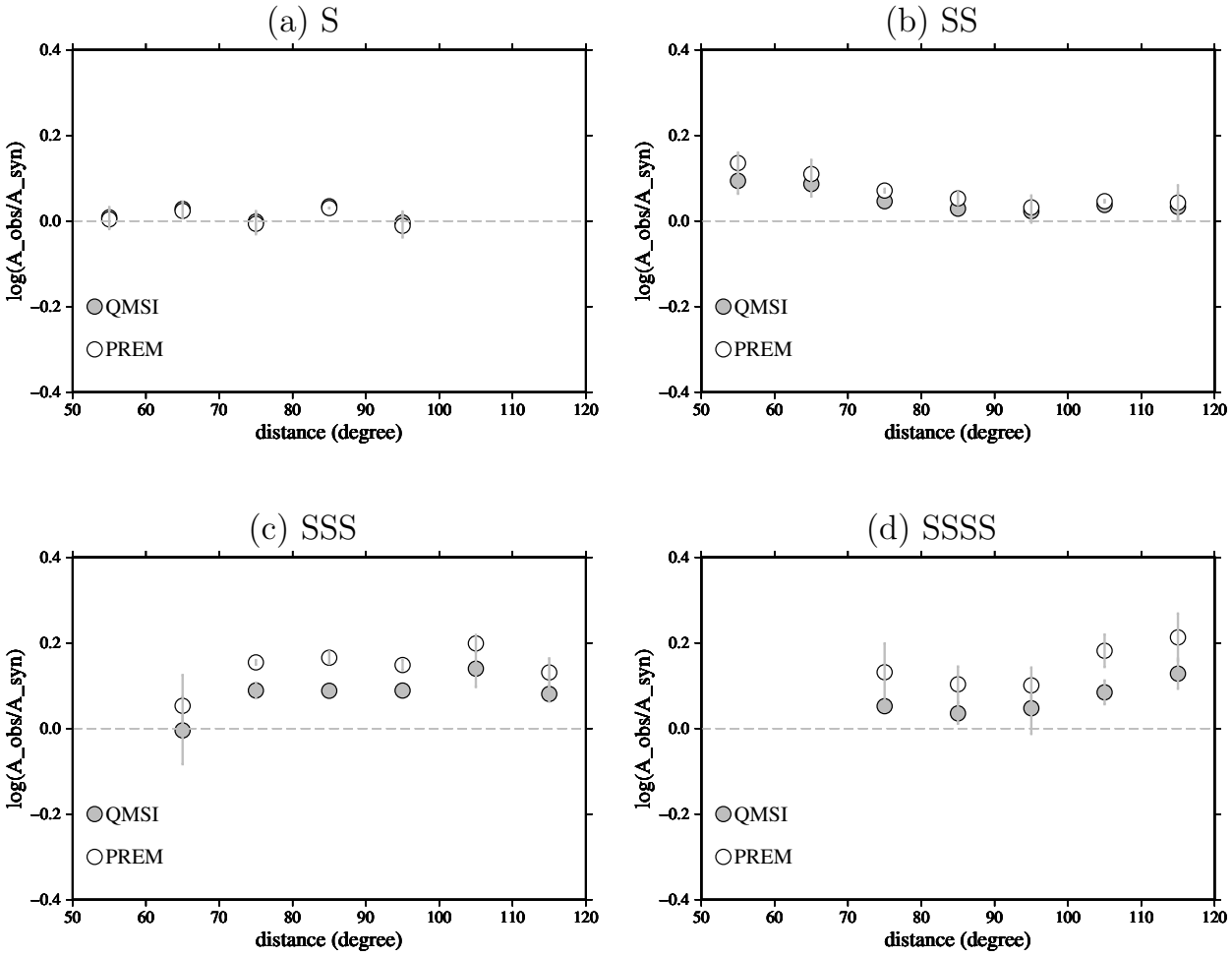

Figure 6. The same as in Figure 4 but for measurements using model QMSI as the reference model (solid circles). The original measurements using PREM as the reference model are plotted in open circles. The mean values are calculated using data within the one standard deviation and the vertical bars indicate the differences between estimates made using data within one standard deviation and two standard deviations. Model QMSI improves the amplitude datafit of SS waves at short epicentral distances as well as the datafit of SSS and SSSS waves that were not used in the linear inversion. Those waves turn at depths roughly between 400 km and 900 km.

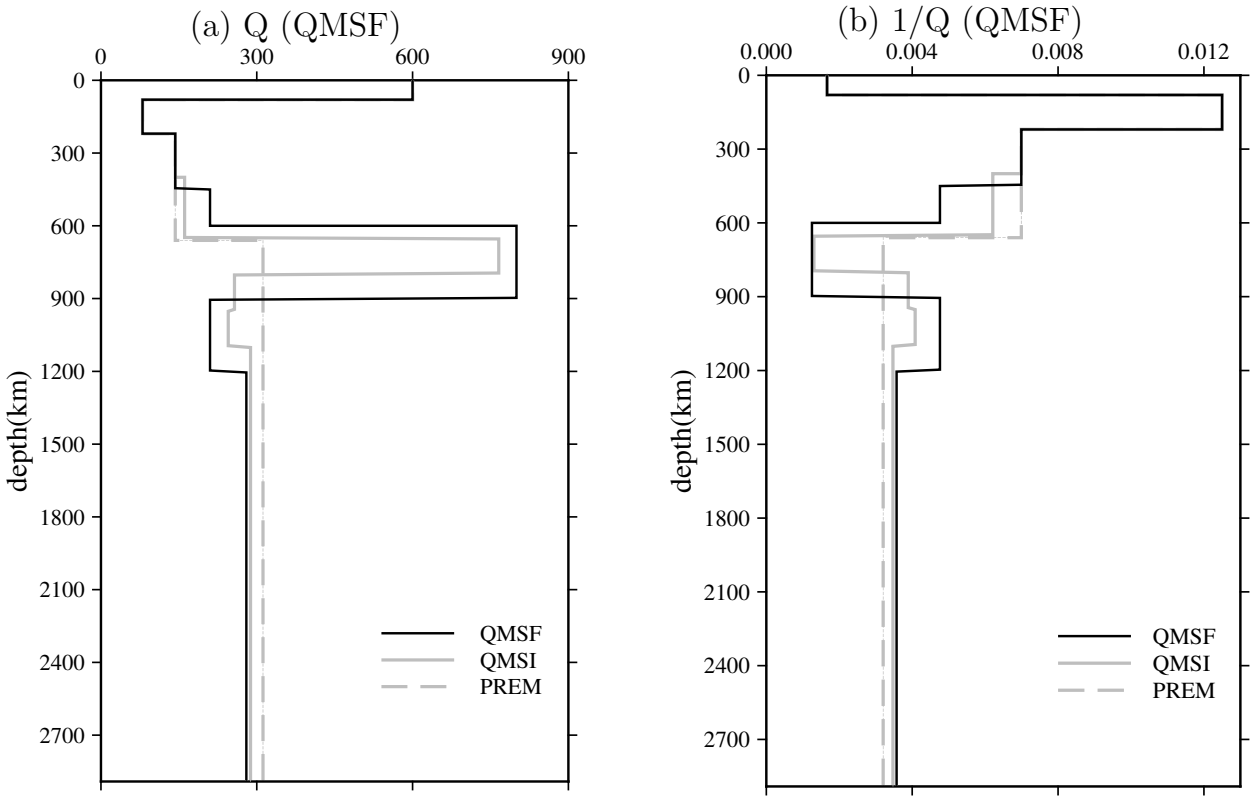

Figure 7. (a) Q Model QMSF obtained from forward modeling using the entire dataset of S, SS, SSS and SSSS amplitude measurements. Models QMSI and PREM are also plotted for reference. (b) The same as (a) but for 1/Q. In forward modeling, we use QMSI as a starting model and adjust Q values to better fit the entire amplitude dataset. The final model (QMSF) requires higher Q values in the mantle transition zone (Q=210 at 450-600 km depth) as well as in the uppermost lower mantle (Q=800 at 600-900 km depth), and lower Q values in the rest of the lower mantle, with Q=210 at 900-1200 km depth and Q=280 at depths greater than 1200 km.

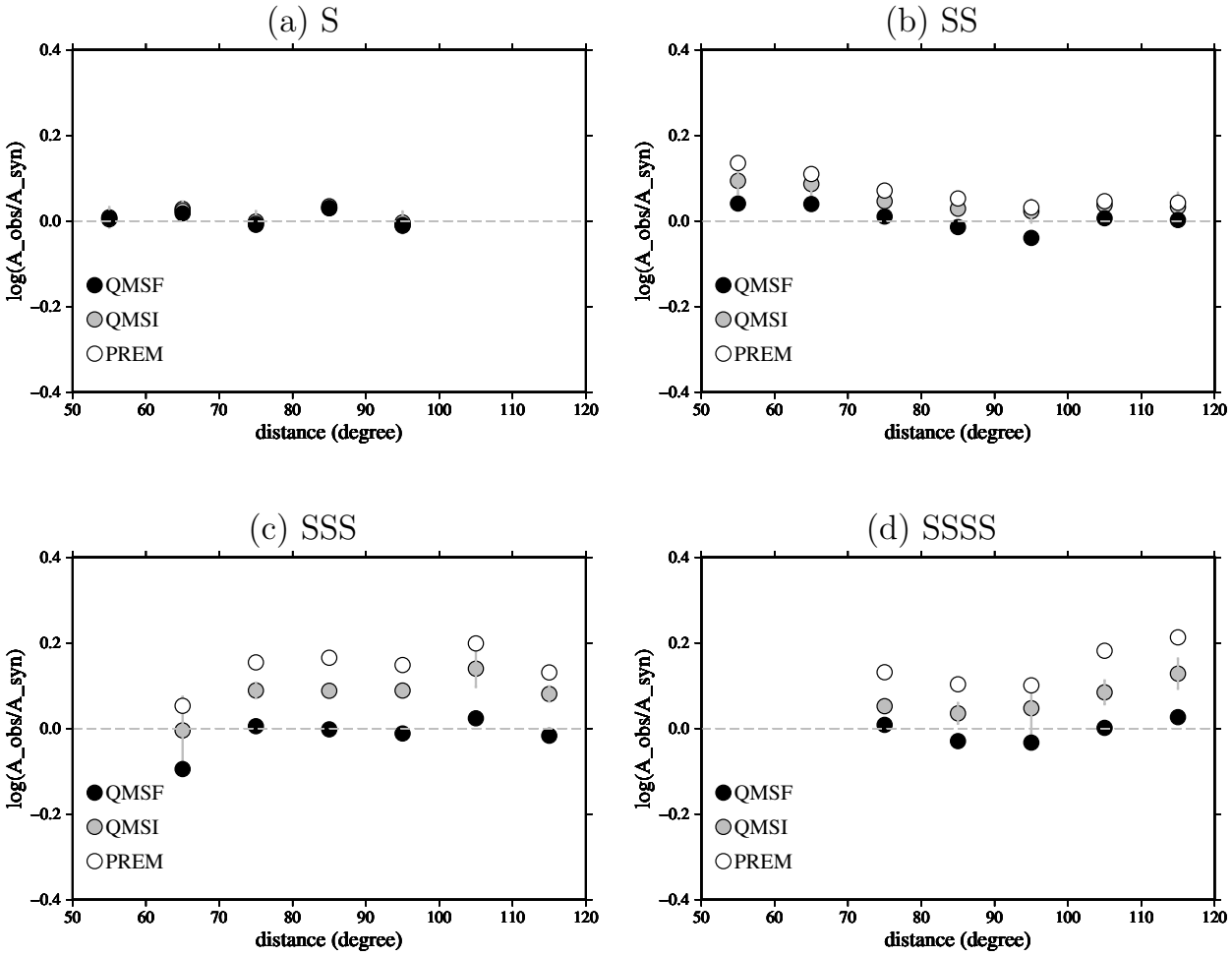

Figure 8. The same as in Figure 4 but for measurements using model QMSF as the reference model. Measurements using models QMSI and PREM are plotted for reference. The high-Q lid in the uppermost lower mantle (600-900 km) improves the amplitude datafit of SS waves at short epicentral distances as well as the datafit of SSS and SSSS waves. The low Q values in the deeper lower mantle were required to fit the S waves and SS waves at larger epicentral distances. The same Figure with running mean average is also plotted in Figure S3 for reference.

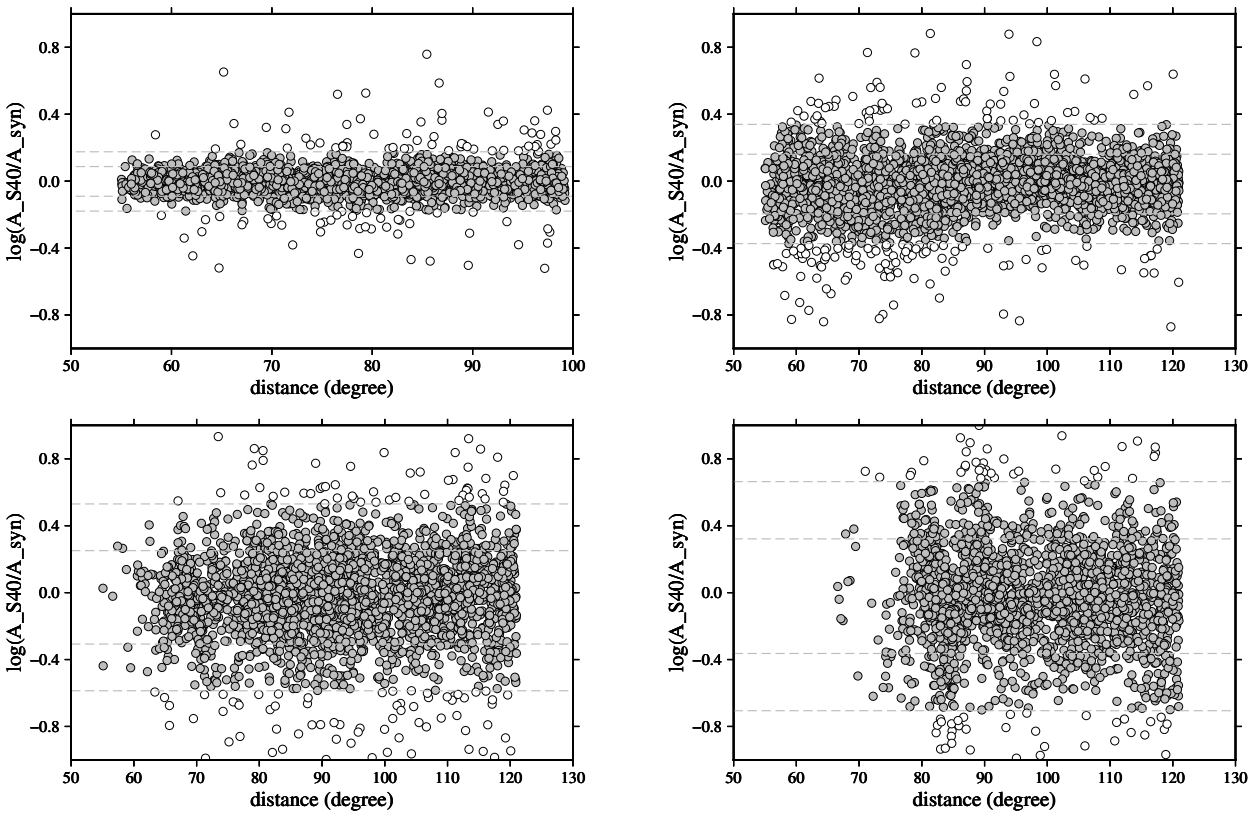

Figure 9. The same as Figure 3 but for synthetic amplitude ratios caused by focusing and defocusing due to mantle wavespeed heterogeneities in a global 3-D mantle model S40RTS. The reference model used in making the measurements is PREM. Synthetic seismograms in model S40RTS and PREM are calculated using SPECFEM3D for the same source-receiver configuration in Figure 3.

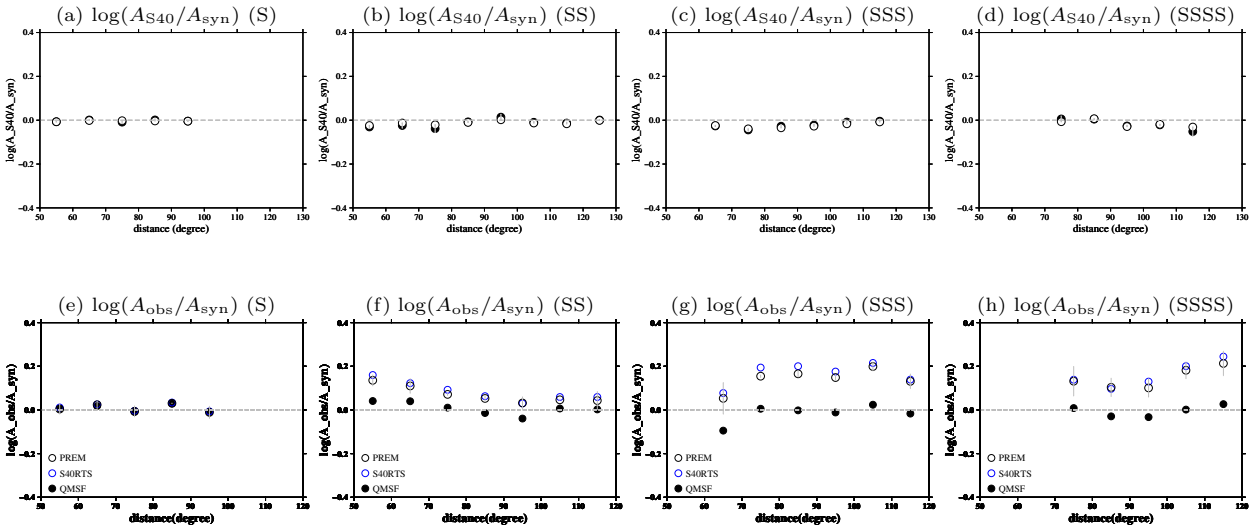

Figure 10. (Top) mean amplitude ratios $\log(A_{\mathrm{S40}}/A_{\mathrm{syn}})$ calculated for the synthetic amplitude ratios in Figure 9 following the same approach as used for real data in Figure 4. (Bottom) mean amplitude ratios as in Figure 8 but now include measurements with respect to references models PREM, S40RTS and QMSF. This Figure shows that variations caused by 3-D mantle wavespeed perturbations through focusing and defocusing does not have a significant impact on the mean amplitudes.

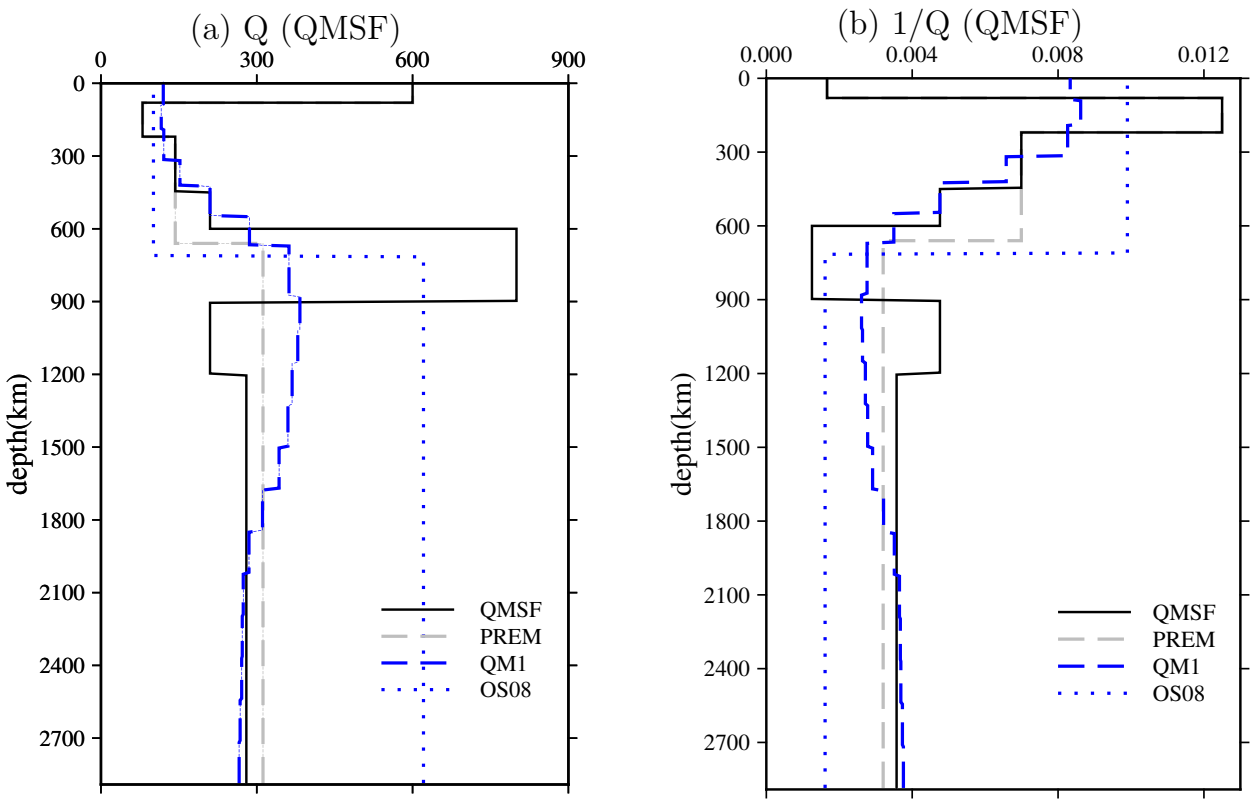

Figure 11. (a) Q model from this study: QMSF (black solid line), plotted with Q models from previous studies that also have high Q values in the uppermost lower mantle: QM1 (Widmer et al. 1991) in blue dashed line and OS08 (Oki & Shearer 2008) in blue dotted line. PREM is plotted in gray dashed line for reference. (b) the same as (a) but for 1/Q.

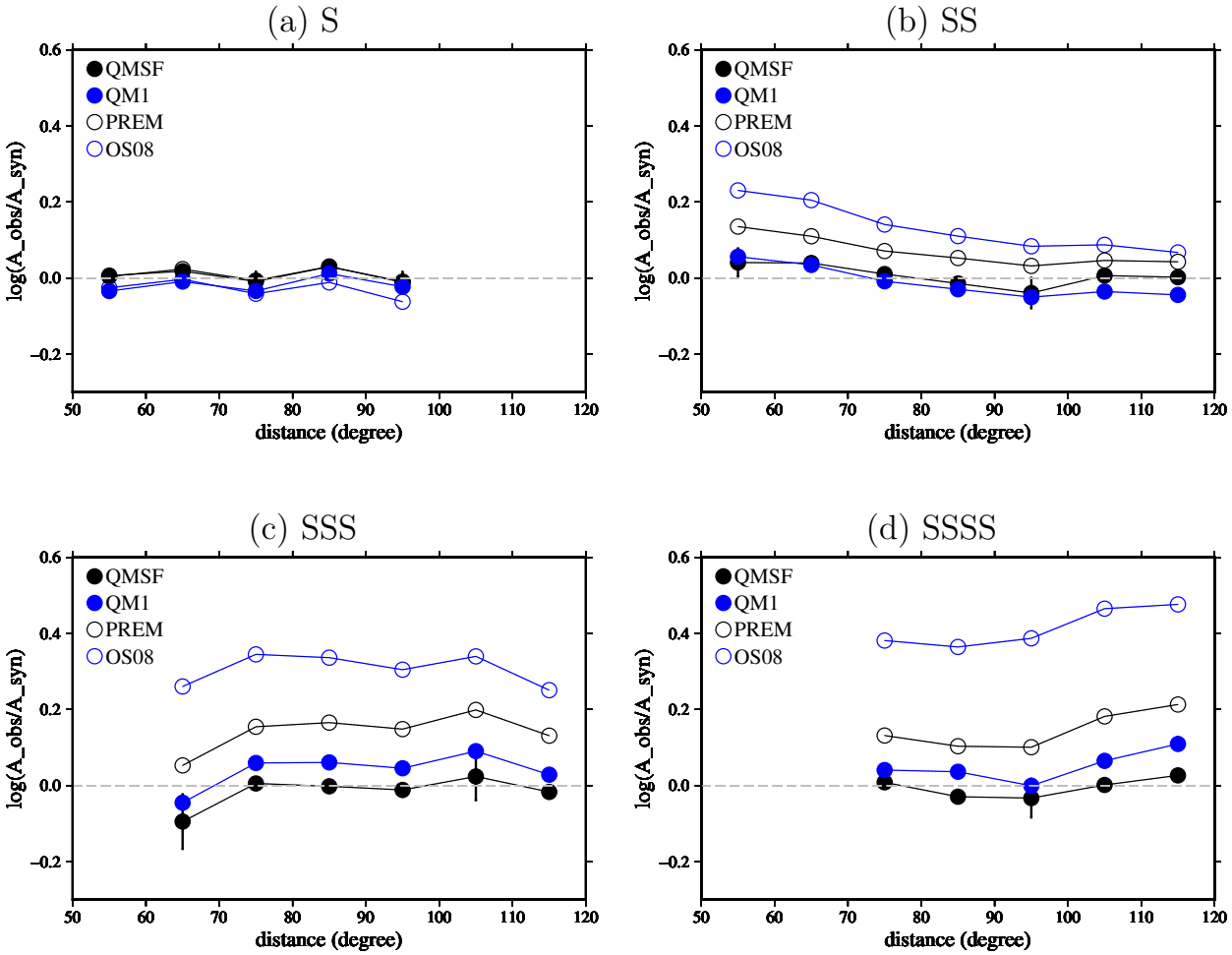

Figure 12. Mean amplitude ratios calculated for different reference models shown in Figure 11.

Mantle Q structure from S, SS, SSS and $SSSS$ amplitude measurements

Geophysical Journal International

Supplemental Information

The Supplemental Information includes 6 Figures (Figure S1-S6).

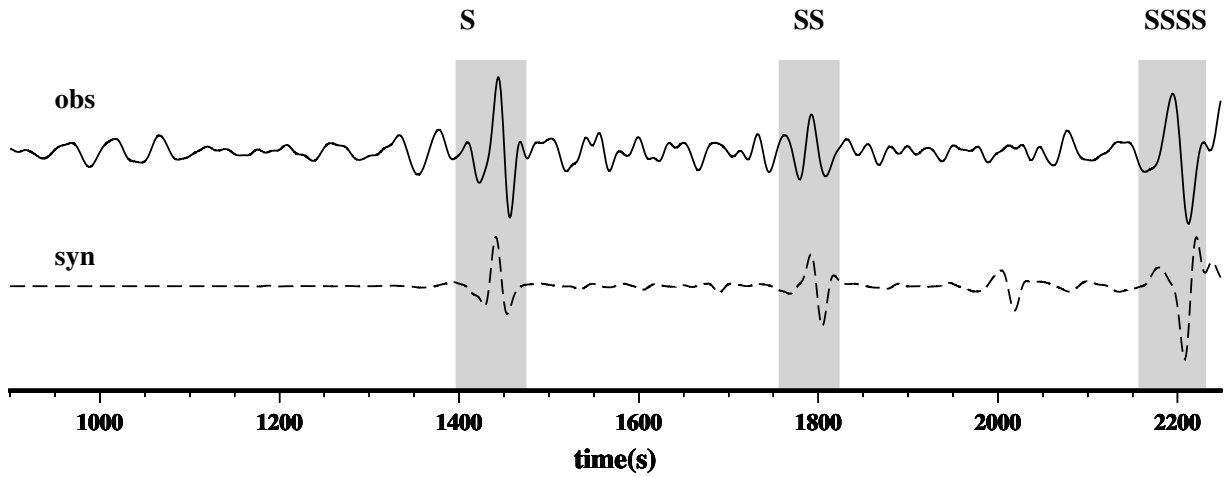

Figure S1: The most noisy seismogram (with the smallest SNR value) used in this study. The signal-to-noise ratio of this observed seismogram is 3.2, defined as the ratio of the maximum amplitude of the S wave divided by the absolute value of the maximum background noise measured in a window 80 seconds prior to the start of the S wave measurement window. The synthetic seismogram is also plotted for reference. The shaded windows indicate measurement windows (S, SS and SSSS) used for this observed seismogram.

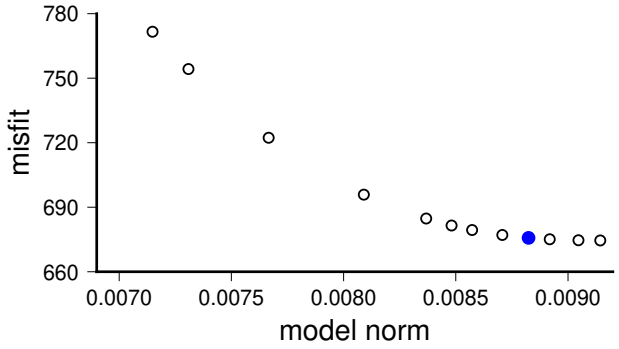

Figure S2: Tradeoff curve of the inverse problem $||\mathbf{Ax} - \mathbf{b}||^2 + \alpha^2||\mathbf{x}||^2 =$ minimum with a varying norm damping parameter α. The horizontal axis is the model norm $||\mathbf{x}||$ and the vertical axis is the misfit $||\mathbf{Ax} - \mathbf{b}||^2$. Model QMSI is indicated by the blue circle where increasing model norm no longer reduces data misfit. Only S and SS wave amplitude measurements are used in this inversion, and the purpose of this inversion is to obtain a model (QMSI) to be used as a starting model in forward modeling.

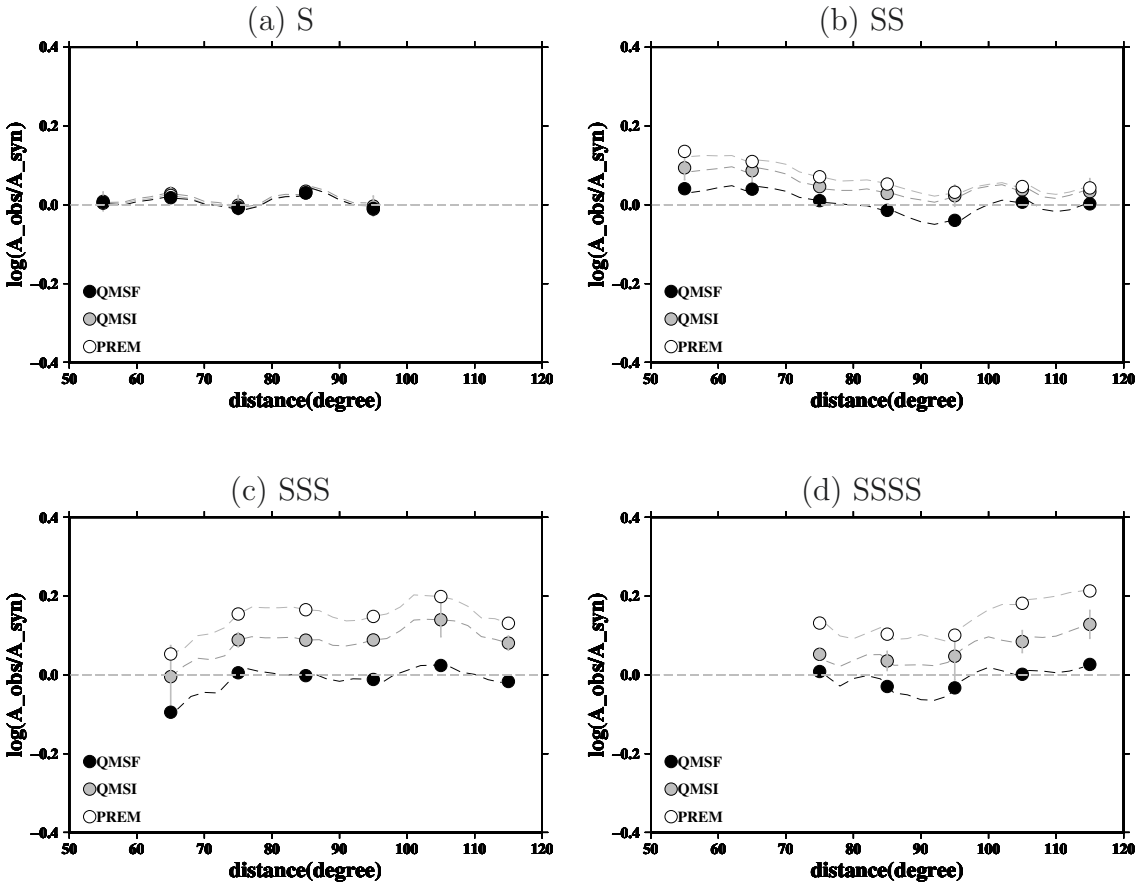

Figure S3: The same as in Figure 8 but with running mean plotted as dashed lines. The circles are independent mean amplitude measurements in every 10° epicentral distance range.

(a) crust thickness (24.4 km & 21 km)

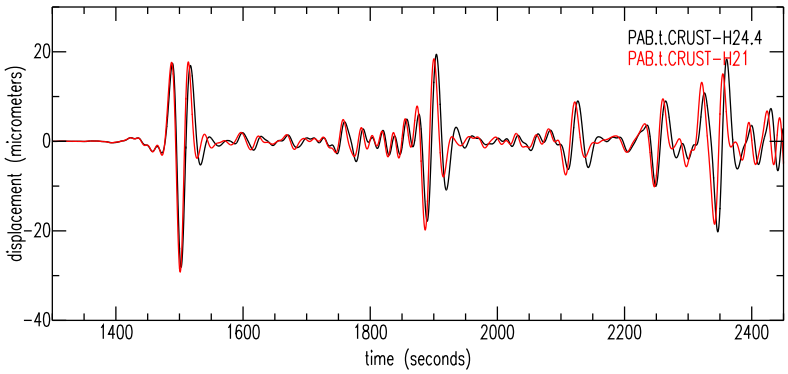

(b) crust thickness (24.4 km & 21 km) - time shifted

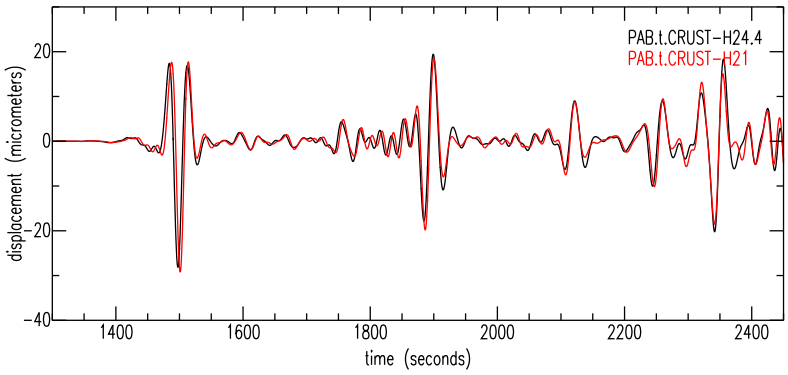

(c) crust thickness (24.4 km & 31 km)

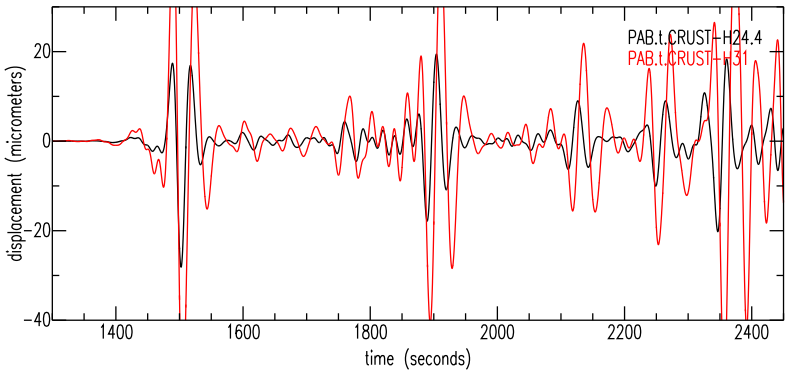

Figure S4: Synthetic seismograms calculated for a moment magnitude Mw=6.9 earthquake off the coast of central Chile recorded at station PAB. The depth of the earthquake is 26 km. The epicentral distance is 95.68° and the S, SS, SSS and SSSS waves arrive at 1478, 1869, 2092 and 2290 seconds, respectively. (a) synthetic seismograms calculated in model PREM with a crust thickness of 24.4 km (black) and in a modified PREM model with a new crust thickness of 21 km (red). The earthquake is located in the mantle in both models. The change in crustal thickness introduces significant traveltime differences on the multiple reflected S waves but there is no significant impact on their amplitudes. (b) The same as (a) but with the black seismogram shifted by 5 seconds for better illustration of the amplitudes of the multiple reflected S waves. (c) The same as (a) but with the red seismogram calculated in a modified PREM model with a new crust thickness of 31 km. The earthquake is located in the mantle in PREM (24.4 km crust) and in the crust in the modified model (31 km crust). This Figure shows that (1) variations in crustal thickness have limited impact on the amplitudes of multiple reflected S waves; and (2) incorporating a 3-D crustal structure with the global CMT solutions can be problematic for source excitations as the CMT solutions are obtained assuming PREM crustal structure, but the local crustal thickness at the source may be different from PREM crustal thickness. All seismograms are calculated in 1-D (not 3-D) crustal models such that the main differences in amplitudes come from source excitation (there is no focusing/defocusing).

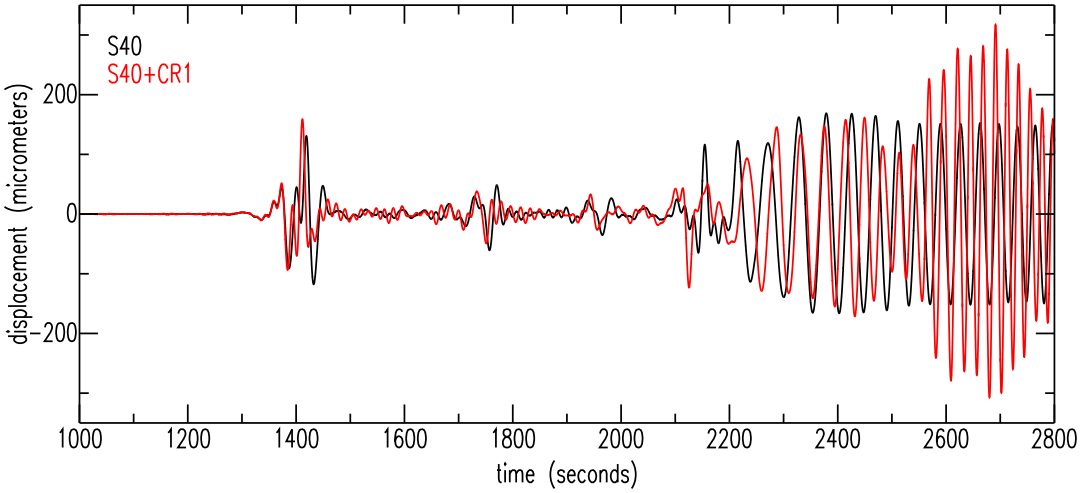

Figure S5: Synthetic seismograms calculated for a Mw=7.2 South Sandwich Islands earthquake in May 2016 recorded at station MTDJ. The depth of the earthquake is 68.7 km. The epicentral distance is 85.65° and the S, SS, SSS and SSSS waves arrive at 1378, 1716, 1928 and 2103 seconds, respectively. The black synthetic seismogram is computed using SPECFEM3D for a 3-D mantle model S40RTS with a 1-D crustal structure (PREM) and the red synthetic seismogram is computed for the same mantle model with a 3-D crust (CRUST1.0). The differences in crustal structure introduce significant phase (traveltime) differences on the (multiple reflected) S waves but there is no significant impact on their amplitudes. The focusing and defocusing effects are generally expected to be small for S waves in global crustal models. This is because unlike the phases (traveltimes) of the seismic waves, their amplitudes are sensitive to the second derivatives of structure perturbations, similar to the focusing effects of a magnifying glass.

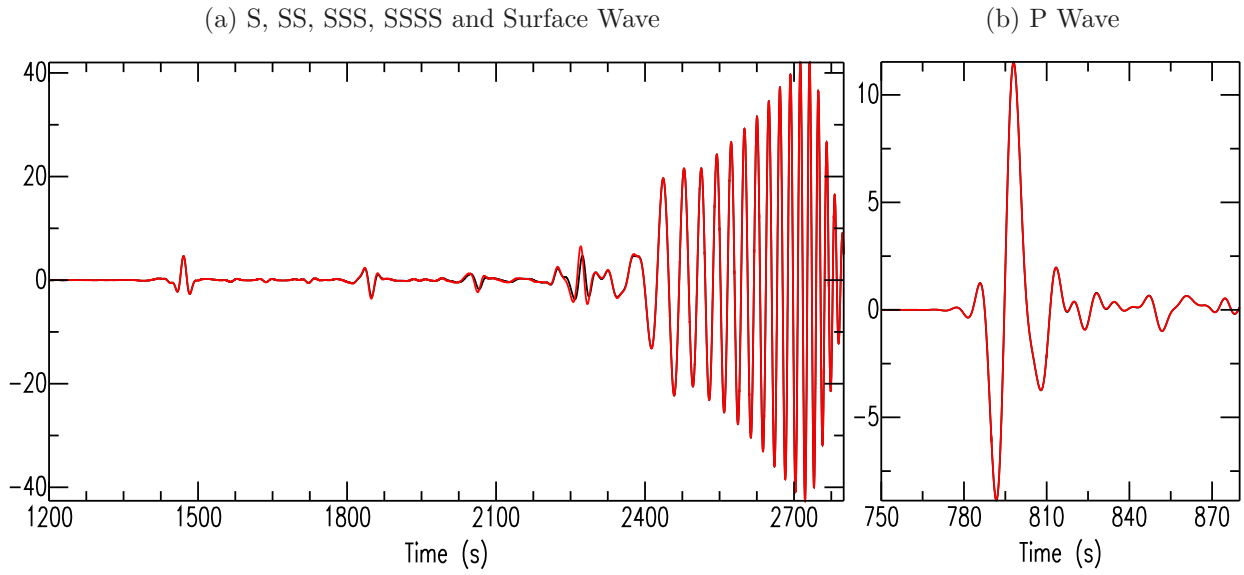

Figure S6: Example synthetic seismograms at station COLA calculated in model PREM (black) and QMSF (red) for a magnitude 6.6 earthquake occurred in 2017 in Loyalty Islands. The differences between model PREM and QMSF are Q values in the mantle transition zone and the lower mantle, which do not have a significant impact on surface-wave or P wave amplitudes.